The Effects of Inoculation on the Weldability of 6061 Aluminum Processed with GMA-DED

A new model incorporating grain size into solidification cracking susceptibility explains the effects of inoculation on weldability

BY J. KLEINDIENST, N. BAGSHAW, J. ITEN, AND J. KLEMM-TOOLE

Abstract

The weldability of plain and inoculated 6061 aluminum processed with gas metal arc directed energy deposition (GMA-DED) was evaluated and compared to wrought 6061. Autogenous gas tungsten arc welds of varying heat inputs were made, and the degree of solidification cracking was evaluated. The degree of cracking in the inoculated 6061 material was lower than that of plain GMA-DED and wrought 6061. Microstructure characterization revealed that the welds on the inoculated 6061 produced fine, equiaxed grains, whereas the plain 6061 showed coarse, columnar grains. A combination of heat transfer and solidification models were employed to predict the solidification morphology of the 6061 welds, which closely matched the experimental results in all cases. A model was developed to understand the effect of grain morphology on solidification cracking, and it was found that equiaxed grains shifted the critical liquid film range for cracking to lower solid fractions where thermal stresses are the lowest. However, cracking can be caused if sufficient external stresses are applied when the critical liquid film thickness is present during solidification of the equiaxed grain structure. This work provides insight into the role grain size and morphology control can have in suppressing solidification cracking of other aluminum alloys.

Keywords

- Gas Metal Arc Directed Energy Deposition
- Weldability
- Wire Arc Additive Manufacturing
- Inoculated
- 6061
- Microstructure Modeling

Introduction

High-strength aluminum alloys, such as 6061 aluminum, are of considerable interest to the aerospace, automotive, and defense industries due to their high strength-to-weight ratio and good corrosion resistance. However, their use in structural applications can be hindered by their weldability problems. Most notably, 6061 is highly susceptible to solidification cracking, which complicates joining by fusion welding processes and often necessitates lower strength fillers, which negates much of the strength advantages of these alloy systems. Solidification cracking occurs when liquid channels rupture between dendrite arms near the end of solidification and cannot be healed by the backfilling of liquid (Ref. 1). Aluminum alloys are especially susceptible to this phenomenon due to their large shrinkage stresses upon solidification (Refs. 2, 3), which develop large strains in the solidifying dendrite network and centerline cracks in welds. Grain size refinement can reduce the susceptibility of an alloy to solidification cracking by distributing the liquid during terminal solidification to a greater number of boundaries, increasing the ease of crack backfilling, and increasing the ability of the microstructure to accommodate strain during solidification without cracking (Ref. 4).

Grain size refinement through inoculation has been shown to eliminate solidification in "unweldable" alloys during welding and additive manufacturing (AM) (Refs. 5–11). An inoculated version of 6061 has recently been used as a wire

Table 1 — Chemical Composition of Wire Feedstocks

Element	Al	Mg	Si	Cu	Fe	Cr	Zn	Mn	Ti	B	C
Plain 6061	Bal.	0.90	0.57	0.19	0.26	0.09	0.00	0.00	0.01	0.004	–
Inoculated 6061	Bal.	1.03	0.63	0.26	0.16	0.13	0.18	0.01	2.00	0.61	0.17

feedstock in gas tungsten arc welding (GTAW) for circumferential groove welds on a high-strength aluminum alloy rocket engine assembly, resulting in a crack-free joint (Ref. 12). Although crack-free welds and AM builds have been made, the improvements in weldability resulting from inoculation have not been quantitatively evaluated.

This work aims to determine how inoculation affects solidification cracking in 6061. Plain and inoculated 6061 aluminum builds and wrought 6061 processed by gas metal arc directed energy deposition (GMA-DED) were evaluated with autogenous GTAW. The weld microstructures were modeled using a combination of heat transfer and solidification models. The knowledge gained from this work can inform the design of new inoculated alloys as well as improve additive manufacturing and welding process development.

Methodology

Test Sample Fabrication

Samples were made by printing single-bead-wide AM walls with GMA-DED. AM walls were made with 0.045-in. plain and inoculated 6061 aluminum welding wires provided by Fortius Metals Inc. The chemical compositions of the wires used are shown in Table 1. The inoculated wire has additions of Ti, B, and C, which react in the melt pool to form nucleation sites (inoculants), termed reactive additive manufacturing (RAM) for grain refinement (Refs. 9, 13). The inoculated wire is available under "A6061-RAM2" from Fortius Metals. A robot-controlled TPS400i GMAW power source using cold metal transfer and a synergic welding line for Al-Mg wire produced the AM builds for both plain 6061 and inoculated 6061 wires. A 100% argon shielding gas was used at a flow rate of 11.3 L/min (30 ft³/h). A travel speed of 12 mm/s (28.3 in./min), a voltage of 12.5 V, and a current of 72 A (I) were used. The single bead-wide walls measured 25.4 cm wide, 15.2 cm tall, and 5.3 mm thick. The walls were machined to plates ⅛ in. (3.175 mm) in thickness and sectioned into 2 in. × 2 in. (50 mm × 50 mm) sections for weldability testing. Commercially available ⅛ in.-thick, 2 in.-wide wrought 6061 in the T6 heat treatment were also used.

Heat Transfer Model

An analytical heat transfer model was used to spatially predict the temperature gradient and solidification velocity at the solid-liquid interface of the melt pools to predict microstructure in the GTA welds. Rosenthal developed analytical heat transfer models for a moving point heat source on a semi-infinite thick plate and a thin plate (Ref. 14). In this case,

the thin plate solution was used because it best matched the experimental conditions of a full penetration weld on a ⅛ in.-thick plate in this study. The model assumes constant thermal conductivity, heat capacity, density, and steady-state heat flow and neglects heat of fusion. The equation for the two-dimensional heat flow, as expressed in (Ref. 4), is:

$$\frac{2\pi(T - T_o)kg}{Q} = exp\left(\frac{Vx}{2\alpha}\right)K_o\left(\frac{Vr}{2\alpha}\right) \tag{1}$$

where T is the temperature, T_o is the starting workpiece temperature, k is the thermal conductivity, g is the workpiece thickness, Q is the heat transferred from the arc to the workpiece, V is the heat source travel speed, a is the thermal diffusivity, K_o is the modified Bessel function of the second kind and zero order, and r is the radial distance from the heat source. Inputs for the model were taken from the literature (Ref. 15). In this study, Q is equal to η*I*V, where η is the heat source efficiency, I is the welding current in amps, and V is the welding potential in volts. To calibrate the heat transfer model to the experimental weld size, the efficiency factor was adjusted to match the simulated weld pool width to the experimental weld pool width. The heat source efficiency η was 0.42, 0.31, and 0.312 for parameter sets 1, 2, and 3, respectively, consistent with the values reported in the literature (Ref. 16). The equation for the thermal diffusivity a is shown in Equation 2:

$$\alpha = \frac{k}{\rho C} \tag{2}$$

where ρ is the density and C is the heat capacity. The equation for the radial distance is shown in Equation 3:

$$r = \sqrt{x^2 + y^2} \tag{3}$$

To calculate the boundary of the melt pool, the equation was solved for when the temperature was equal to the liquidus temperature of 6061 aluminum, 652°C. Then, temperature values were calculated slightly offset from the melt pool boundary in both the x and y directions. Using these values, the temperature gradient was estimated by dividing the change in temperature by the change in distance. The cooling rate was calculated by dividing the change in temperature along the travel direction by the change in time using the travel speed. The solidification velocity perpendicular to the solid-liquid interface was approximated using V = C/G, where

Table 2 — Input Parameters for Thin-Plate Rosenthal Model

Parameter	Symbol (Units)	Value
Density (Ref. 15)	ρ (kg/m³)	2700
Heat Capacity (Ref. 15)	c (J/kgK)	896
Thermal Conductivity (Ref. 15)	k (W/mK)	167
Liquidus Temperature	T_l (K)	925
Initial Temperature	T_o (K)	300
Arc Thermal Efficiency	η (%)	varied
Arc Power	Q (W)	varied
Travel Velocity	V (mm/s)	varied
Wall Thickness	g (mm)	3.183

V is the solidification velocity, C is the cooling rate, and G is the temperature gradient.

The individual solidification velocities and temperature gradients were then calculated along the entire solidifying edge of the melt pool and used to predict the solidification microstructure of the welds. This methodology has been applied to this alloy and inoculation system processed with GMA-DED build to successfully predict the solidification microstructure (Ref. 17). The constants used in the heat transfer model for 6061 are shown in Table 2, where all the thermophysical properties are for the solid at room temperature.

Microstructure Development Models

This study's microstructure development models used to predict solidification structure were the Ivantsov marginal stability (IMS) model for dendritic growth and the columnar to equiaxed transition (CET) model. IMS analytically models a growing dendrite tip as a parabolic needle in a diffusional field (Refs. 17–19). The following equations were used in this model:

$$4\pi\Gamma\left(\frac{1}{R^2}\right) + \left(2\sum[m_i Pe_i(1-k_i)C_i^*\xi_i]\right)\left(\frac{1}{R}\right) + G = 0 \tag{4}$$

$$\xi_i = 1 - \frac{2k_i}{\sqrt{1+\left(\frac{2\pi}{Pe_i}\right)^2}-1+2k_i} \tag{5}$$

$$C_i^* = \frac{C_o}{1-[(1-k_i)Iv(Pe_i)]} \tag{6}$$

$$Pe_i = \frac{RV}{2D_i} \tag{7}$$

where R is the dendrite tip radius; m_i is the liquidus slope for a solute element; Pe_i is the Peclet number for a solute; k_i is the partition coefficient for a solute; Γ is the Gibbs-Thomson coefficient; C_i^* is the composition of a solute in the liquid at the dendrite tip; ξ_i is a stability parameter; V is solidification velocity; G is the temperature gradient; D_i is the interdiffusion coefficient of a solute in the liquid; C_o is the bulk composition of a solute; and I_v is the Ivantsov function. The total undercooling in front of a moving dendrite tip can be found using Equations 8–10 by summing the undercooling additions of each solute element and the curvature undercooling of the dendrite tip.

$$\Delta T_{c,i} = m_i(C_o - C_i^*) \tag{8}$$

$$\Delta T_R = \frac{2\Gamma}{R} \tag{9}$$

$$\Delta T_{Total} = \sum_i \Delta T_{c,i} + \Delta T_R \tag{10}$$

In Equations 8 through 10, ΔT_{Total} is the total undercooling; $\Delta T_{c,i}$ is the constitutional undercooling from a solute; and ΔT_R is the curvature undercooling. The IMS model assumes linear liquidus slopes, constant solute diffusivities, and partitioning coefficients to simplify calculations. The inputs for the

Table 3 — Values Used for IMS Dendrite Growth Model of 6061

Solute	D (m²/s) (Ref. 20)	k (unitless)	m (K/wt-%)
Mg	8.96E-9	0.287	−4.79
Si	2.71E-9	0.095	−5.55
Cu	4.68E-9	0.095	−2.40
Cr	3.56E-9	5.20	0.47
Ti	3.82E-9	9.78	27.3

Table 4 — GTAW Parameters for Weldability Testing

	Travel Speed (m/s)	Welding Current (A)	Welding Voltage (V)	CTTWD (mm)	Heat Input (kJ/m)
Parameter 1	0.0508	200	~14.9	~1	586.6
Parameter 2	0.012	275	~18.5	~1	424.4
Parameter 3	0.022	330	~19.8	~1.5	296.8

equations are shown in Table 3. The values of solute diffusivity (D_i) for the major alloying elements in the inoculated 6061 alloy evaluated here were taken from the literature (Ref. 20), and the values of the partitioning coefficient (k_i) and liquidus slope (m_i) were determined from single-axis equilibrium simulations in Thermo-Calc version 2023b using the TCAL7 database. A Gibbs-Thompson coefficient (Γ) of 1.0E-7 K/m, taken from the literature (Ref. 21), was also used. Thermo-Calc was also used to perform Scheil simulations for the discussion section.

Two IMS models were developed based on Equations 4–10, one for each sample type: plain 6061 and inoculated 6061. While the primary alloying elements were assumed to remain constant for both sample compositions, the inoculated 6061 featured additional constitutional undercooling due to its higher Ti content. The IMS model provided total undercooling and dendrite tip radius as a function of solidification velocity, which were subsequently used as inputs for the microstructure model.

In addition to the IMS model, the CET model was used to predict new grain nucleation during solidification (Ref. 17). The CET model was developed by Hunt (Ref. 22), and a modification by Gäumann was used here (Ref. 23). The following equations were used for the CET model:

$$G = \frac{1}{n+1} \sqrt[3]{\frac{-4\pi N_o}{3 \ln(1-\phi)}} \Delta T_{Total} \left(1 - \frac{\Delta T_{nuc}^{n+1}}{\Delta T_{Total}^{n+1}}\right) \tag{11}$$

$$\Delta T_{Total} = (aV)^{\frac{1}{n}} \tag{12}$$

$$N_o = \frac{1}{\sqrt[3]{grain\ size}} \tag{13}$$

$$\Delta T_{nuc} = \frac{2\Gamma}{r} \tag{14}$$

where N_o is the nucleation site density of an alloy; Φ is the volume fraction of equiaxed grains; a and n are fitting parameters of the power law relationship between total undercooling and velocity; ΔT_{nuc} is the required activation undercooling for a nucleation site; and r is the radius of nucleation site. Nucleation site density cannot be reliably predicted in advance and was determined from the grain size of the GTA welds and the relationship in Equation 13 (Ref. 18). The CET model depends on the volume fraction of equiaxed grains (Φ), but this value is challenging to measure directly from microstructure images. Hunt proposed that a fully equiaxed microstructure corresponds to a volume fraction of 0.49, while the transition from columnar to equiaxed begins at 0.0066 (Ref. 22). For this study, these values were rounded to 0.5 and 0.01, respectively.

Weldability Experimentation

For the weldability test, autogenous gas tungsten arc welds were made on the 6061 aluminum plates with the parameters shown in Table 4. A Miller Dynasty® 350 power source was used with the GTAW torch on a motorized track for consistent
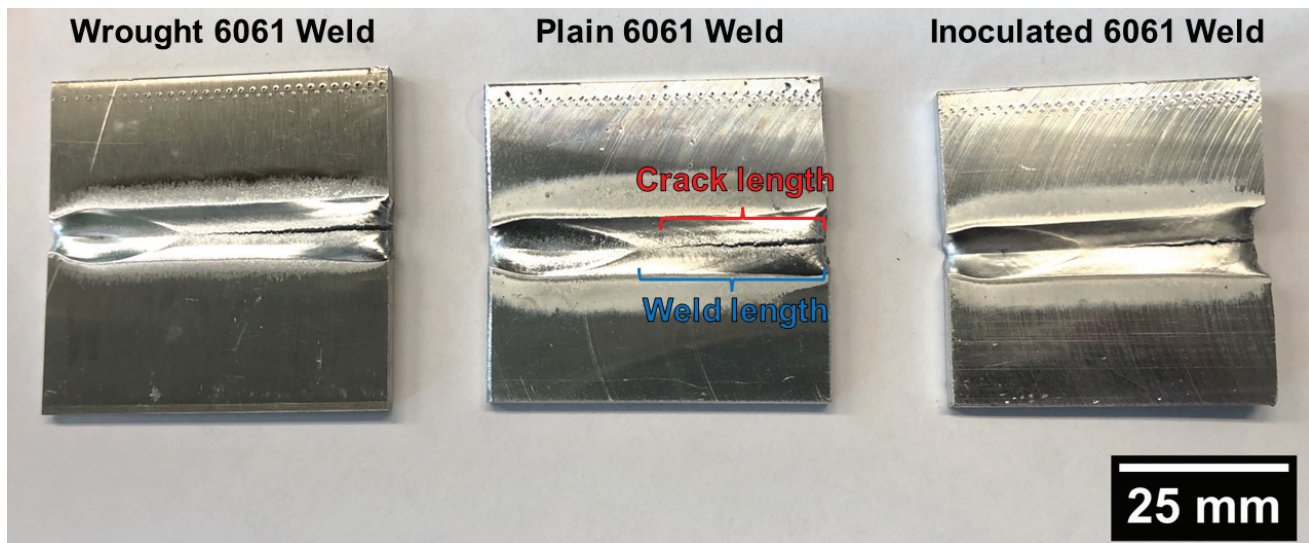
Fig. 1 — Photo of representative samples welded with parameter set 2 (424.4 kJ/m). The relevant dimensions used to calculate % cracking are shown in the center photo.

travel speed and contact tip-to-work distance (CTTWD). A ³⁄₃₂ in. diameter 2% lanthanated tungsten rod ground to a 45 deg angle was used, and 100% argon shielding gas was used at a flow rate of 11.3 L/min (30 ft³/h). Three replicates of each parameter set with different travel speeds and arc powers were used to investigate the effects of processing parameters on weldability in the 6061 aluminum system. Each parameter set achieved a full penetration weld on the ⅛ in.-thick plates. Prior to welding, the dimensions of the plates were measured, and acetone was used to clean the surface of the plates. The plates were clamped across the width on one edge of the plate, with the rest free-floating. The weld was started on one edge of the plate, and the arc was extinguished when the melt pool reached the other end. Three welds were made for each base material with each parameter set. The welds were recorded using a Xiris XIR-1800 short wavelength infrared thermal camera.

The welding voltage was observed during welding and the average value was recorded. A larger CTTWD was used in parameter set three as the arc tended to penetrate through the workpiece at the beginning of welding, so the CTTWD was increased to spread out the arc and manage the heat source power density. The heat was calculated using Equation 15 (Ref. 24):

$$HI = \frac{I * V}{TS} \qquad (15)$$

where I is the welding current, V is the welding voltage, and TS is the welding travel speed. To quantify the amount of cracking in each weld test, a % cracking metric was used. The crack length was measured and then normalized by the length of the weld excluding the end crater, as shown in Fig. 1. Analysis of variance was performed to determine what experimental variables had a statistically significant influence on % cracking using the Minitab software package. An observed level of significance, or p value, less than 0.05 was considered statistically significant.

Microstructure Characterization

The GTA welds were cross-sectioned perpendicular to the welding direction and polished down to 0.05 μm colloidal silica. Electron backscatter diffraction (EBSD) was conducted on the samples to evaluate the grain structure and morphology. A FEI Helios 600i SEM/FIB microscope was used, and EBSD was conducted with a beam energy of 20 keV and a beam current of 11 nA, and neighbor pattern averaging and reindexing was used post-process to clean the EBSD scans. The criterion for a grain was a misorientation of at least 5 deg, and grain size was the area-averaged grain size.

Results

Cracking Results

All materials and processing parameters displayed solidification cracking spanning from the start of the weld and continuing along the melt pool centerline, as shown in Fig. 1. Images taken during the tests from the thermal camera showed that the cracks initiated when the melt pool began to solidify at the edge of the sample and propagated as the trailing edge of the melt pool moved across the sample, as shown in Fig. 2. The observation that cracking began toward the end of solidification at the centerline of the weld provided strong evidence that solidification cracking was the observed mechanism, which would be expected considering 6061 is highly susceptible.

The average melt pool widths of the GTA welds made with each parameter set were measured and are shown in Table 5. No difference in melt pool dimensions was observed across the three materials with welds with the same parameters. Melt pool width decreased from parameter set one to three, which corresponded to the decrease in heat input.

The influence of material type and welding parameter set on % cracking is shown in Fig 3. The inoculated GMA-DED
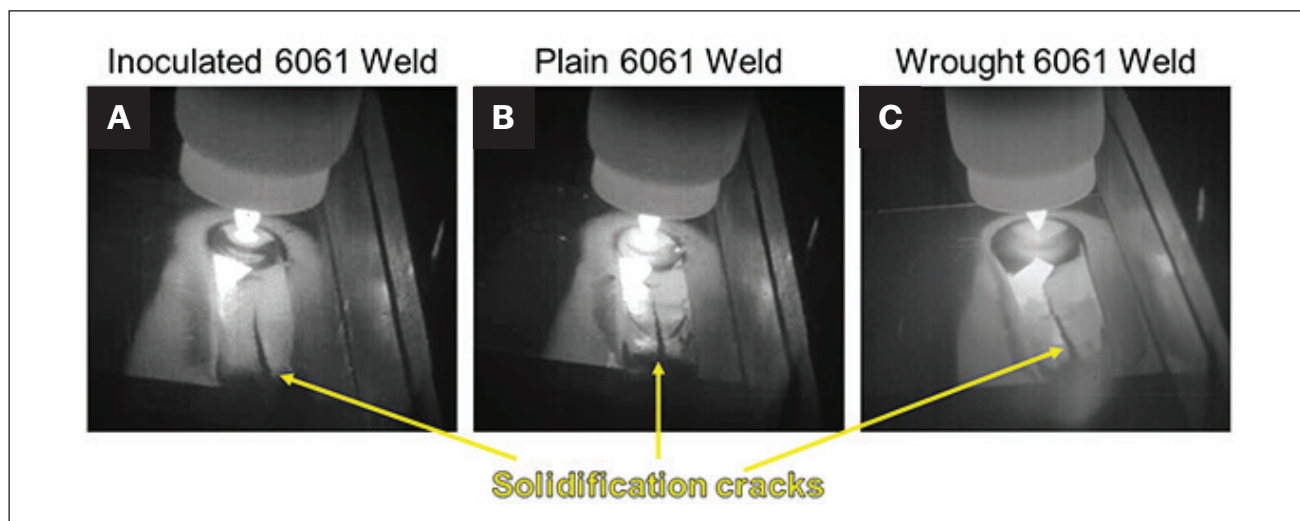
Fig. 2 — In-situ thermal camera images of solidification cracks propagating along the centerline of the welds. The image contrast is infrared emission.

Table 5 — Average Melt Pool Widths of GTA Welds			
	Parameter 1 (586.6 kJ/m)	Parameter 2 (424.4 kJ/m)	Parameter 3 (296.8 kJ/m)
Melt Pool Width (mm)	12.5	8.1	6.7

6061 material showed a statistically significant reduction in cracking compared to both the plain GMA-DED 6061 and wrought 6061 materials, as indicated by a p value of 0.00 (Fig. 3A). However, there was no significant difference in the degree of cracking between the plain GMA-DED 6061 and wrought 6061 materials. There was no statistically significant difference in the cracking response between the welding conditions evaluated, as shown in Fig. 3B.

The extent of cracking for each combination of material and welding parameter set is shown in Fig 4. As shown in Fig. 3A, the wrought and plain GMA-DED 6061 showed the same cracking behavior across parameter sets. However, the inoculated GMA-DED 6061 showed a slightly greater degree of cracking at the highest heat input, such that there was no statistically significant difference between the degree of cracking in three materials in the highest heat input welding parameter. At lower heat inputs, the degree of cracking was lower in the inoculated GMA-DED condition compared to wrought and plain GMA-DED.

Weld Microstructure

The as-solidified grain structure of GTA welds on the inoculated and plain GMA-DED 6061 is shown in Fig 5. The EBSD scans shown in Fig. 5 were taken near the centerline crack, and the grain size was measured. The inoculated plate welds displayed a near-equiaxed, fine grain microstructure. Average grain sizes in the GTA weld of the inoculated GMA-DED sample were 21.7 $\pm$ 1.1 µm, 23.1 $\pm$ 1.2 µm, and 27.2 $\pm$ 1.3 µm when welded with parameter 1 (586.6 kJ/m), 2 (424.4 kJ/m), and 3 (296.8 kJ/m), respectively. The grain sizes in the GTA welds were within the range observed in the inoculated GMA-DED plates themselves, indicating that the inoculation continued to be effective at grain refinement during subsequent melting and re-solidification. The average grain sizes of the plain GMA-DED 6061 materials were 214 $\pm$ 11 µm, 303 $\pm$ 15 µm, and 282 $\pm$ 14 µm when welded with parameters 1 (586.6 kJ/m), 2 (424.4 kJ/m), and 3 (296.8 kJ/m), respectively. Grains in the GTA weld of the GMA-DED 6061 material were large. They tended to extend along the direction of solidification, except those made with parameter set 1 in Fig. 5D, which showed a less-elongated grain structure. The less-elongated appearance of welds made with parameter set 1 was likely due to the weld pool being elliptical as opposed to the teardrop-shaped pools in parameter sets 2 and 3. The grains were likely of similar size in parameter 1 compared to the other welding conditions. However, they were oriented into the plane of the EBSD scan, as grains curve over and follow the direction of welding in an elliptical weld pool near the melt pool's centerline, where these maps were taken. In general, the grain sizes in the GTA welds of both plain and inoculated GMA-DED materials increased from parameter sets 1 to 3.

Solidification Microstructure Modeling

The temperature gradient and velocity of the solid liquid interface during solidification of each GTAW parameter set
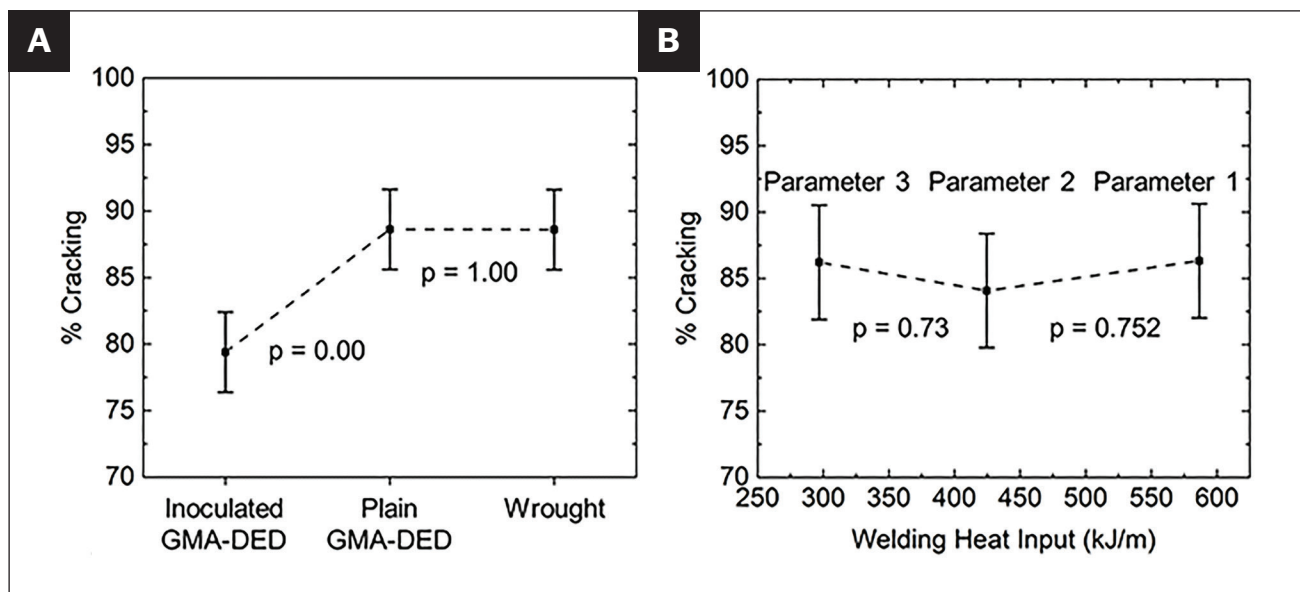
Fig. 3 — Interval plots with 95% confidence intervals showing the effects of: A — Material; B — welding parameters on % cracking.
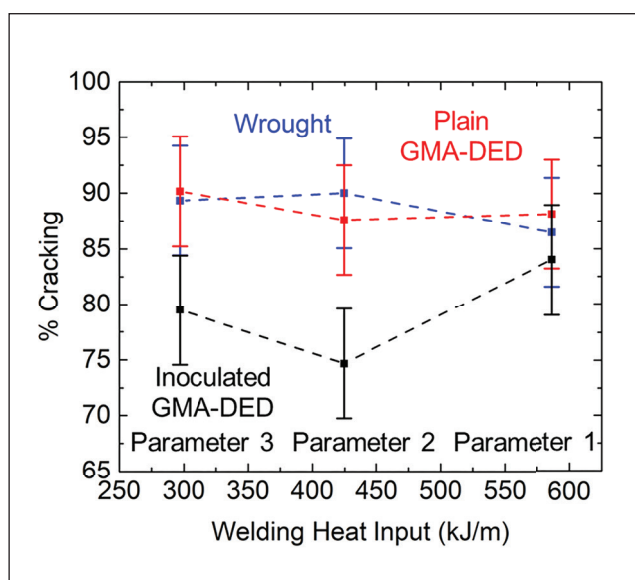

Fig. 4 — Interval plot with 95% confidence intervals of % cracking for each combination of material and welding parameter set evaluated.

from the thin plate Rosenthal heat transfer model are plotted with CET curves in Fig. 6. The predicted solidification microstructure of the GTA welds on plain GMA-DED 6061 samples are shown in Fig. 6A. The GTA welds from all three parameter sets for these samples were expected to have a columnar dendritic microstructure, which matched the experimental grain maps shown in Fig. 5. While a small amount of new grain nucleation was predicted at the middle of the melt pool, little grain refinement was likely to result. It is difficult to characterize the center of the GTA welds due to the prominent centerline solidification cracks. Microstructure predictions for the GTA welds on the inoculated GMA-DED materials are

displayed in Fig. 6B. The majority of each of the welds in Fig. 6B were predicted to have a fully equiaxed microstructure. The microstructure predictions shown in Fig. 6B matched the grain structures of these conditions shown in Fig. 5. Although the CET model used here cannot directly predict grain size per se, it can be seen that a greater portion of the melt pools in the higher heat input parameters (i.e., 1 vs. 3) were past the prediction of 50% equiaxed grains, indicating a greater amount of new grain nucleation was expected. A greater amount of new grain nucleation would indicate that finer grains should result. The higher heat input parameters predicted to have more new grain nucleation show finer grain sizes in Fig. 5. Overall, microstructure predictions of the GTA welds on the plain and inoculated GMA-DED samples matched the experimental results.

Discussion

Combined Effects of Heat Input and Microstructure on Crack Susceptibility

The results of this work show that inoculation remains effective at grain size refinement in autogenous GTA welds made across a range of heat inputs. Furthermore, GTA welds on the inoculated GMA-DED 6061 showed a lesser degree of cracking compared to plain GMA-DED and wrought 6061. However, the highest heat input condition that displayed the finest grain size showed cracking behavior comparable to plain GMA-DED and wrought 6061 that possessed coarse columnar grains. It is likely that the highest heat input condition resulted in higher tensile stresses/strains during solidification compared to the other welding parameters, leading to a greater amount of cracking. Table 5 shows that the highest heat input weld had the widest melt pool, which leads to the largest thermal and solidification shrinkage strains,
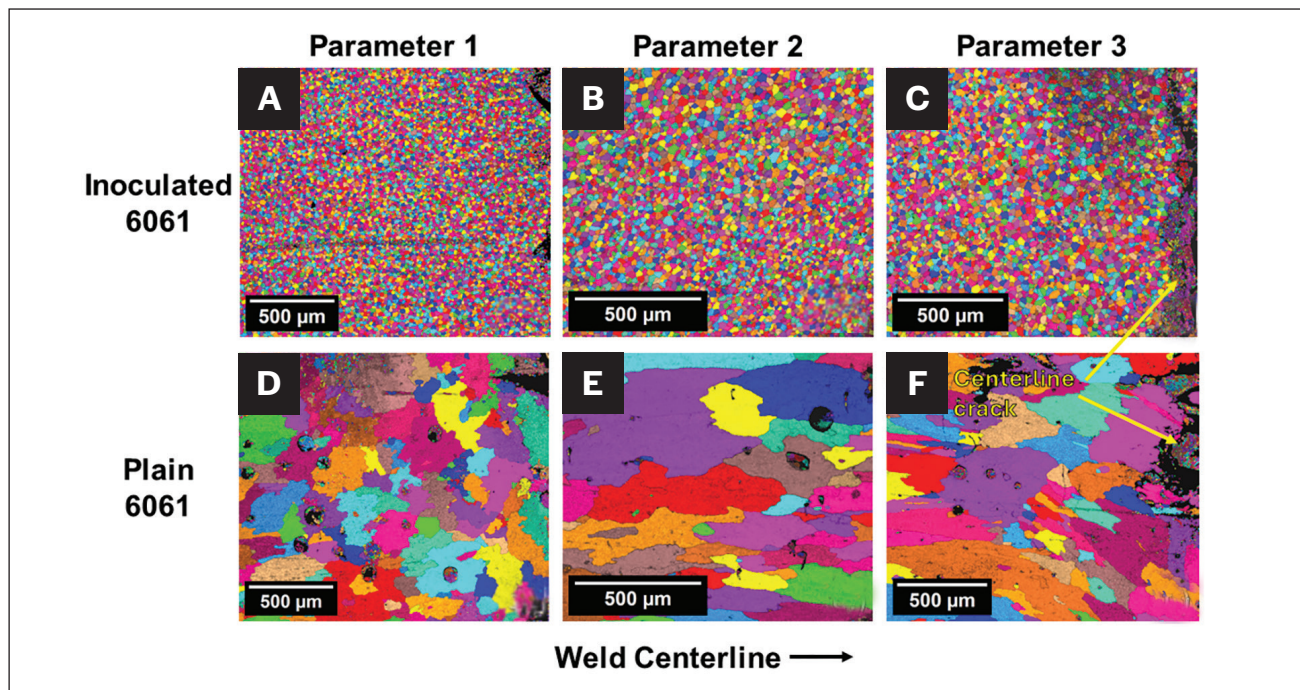
Fig. 5 — EBSD unique grain color maps of the centerline of GTA welds on: A — Inoculated GMA-DED welded with parameter set 1 (586.6 kJ/m); B — inoculated GMA-DED welded with parameter set 2 (424.6 kJ/m); C — inoculated GMA-DED welded with parameter set 3 (296.8 kJ/m); D — plain GMA-DED welded with parameter set 1; E — plain GMA-DED welded with parameter set 2; F — plain GMA-DED welded with parameter set 3.
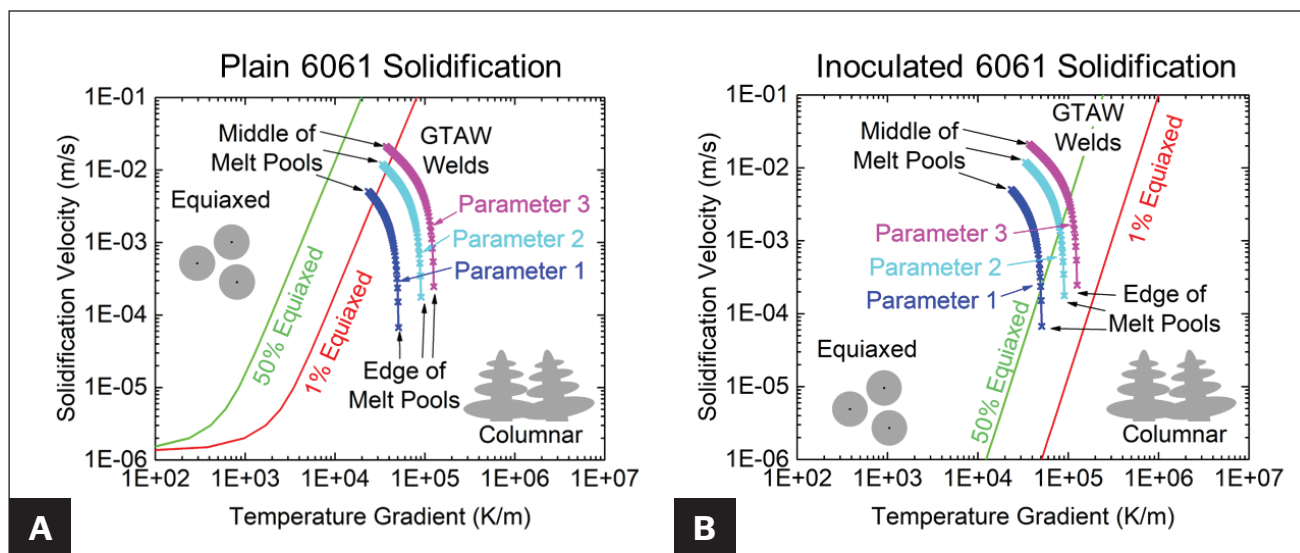

Fig. 6 — Solidification microstructure prediction maps showing the amount of new grain nucleation from a CET model in GTA welds on: A — Plain GMA-DED 6061; B — inoculated GMA-DED 6061 materials.

which leads to higher tensile stresses. These elevated tensile stresses must be high enough to induce a cracking response in the equiaxed microstructure similar to that in the plain 6061 welds.

It has been established in the literature that fine grain, equiaxed microstructures are less susceptible to solidification cracking than a columnar microstructure (Ref. 8). However, the relationship between the degree of grain refine-ment, the stresses present during the solidification, and the suppression of solidification cracking remains somewhat ambiguous. Here, a new model has been developed to pro-vide some insight. Expressions were developed to relate the average liquid film thickness as a function of fraction solid for columnar and equiaxed microstructures similar to those observed in this work. The basis for these expressions is the following relationship:
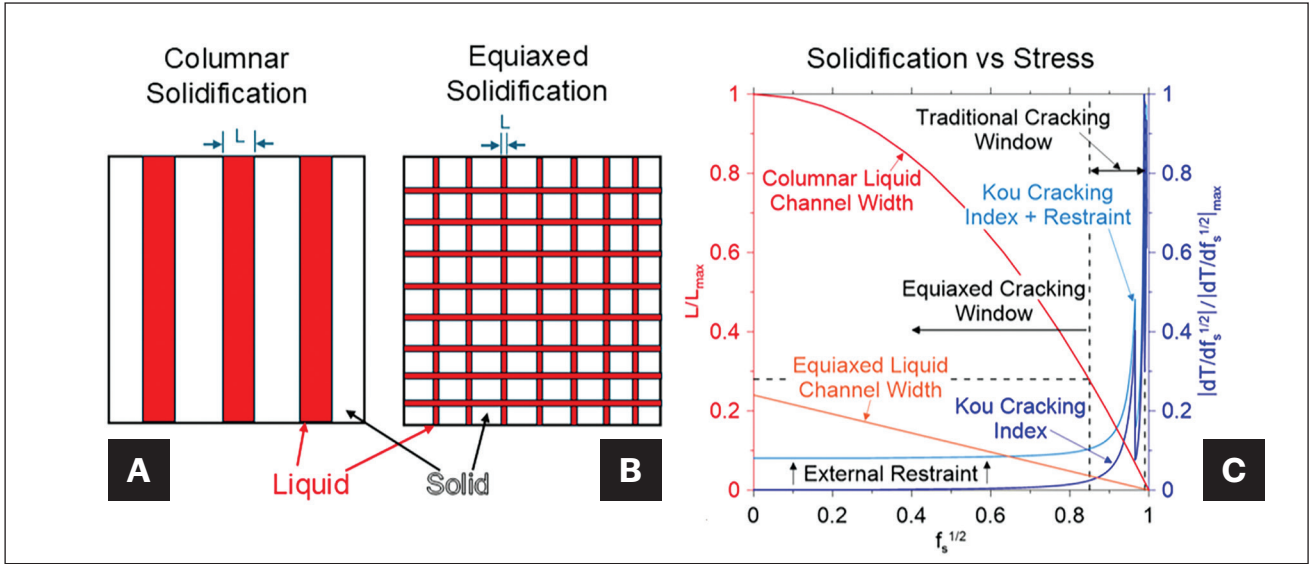
Fig. 7 — Model illustrating liquid film thickness during solidification for: A — Columnar; B — equiaxed solidification morphology; C — the relationship between liquid film thickness and thermal stresses as solidification proceeds.

$$f_s = 1 - \frac{A_L}{A_{tot}} \qquad (16)$$

where f_s is the fraction solid, A_L is the area of the liquid films, and A_{tot} is the total area considered in a two-dimensional representation shown in Figs. 7A and B. From this expression, the relationship for columnar solidification can be found as:

$$f_s = 1 - \frac{\frac{x}{g}Lx}{x^2} \qquad (17)$$

which can be simplified to:

$$L = g(1 - f_s) \qquad (18)$$

where L is the thickness of liquid channels, x is the dimension of a square area considered, and g is the average grain width in the solidification microstructure. For an equiaxed microstructure, the grains were assumed to be square in shape and the following expression was developed:

$$f_s = 1 - \frac{2\frac{x}{g}Lx - \left(\frac{x}{g}L\right)^2}{x^2} \qquad (19)$$

which can be simplified to:

$$L = g\left(1 \pm \sqrt{f_s}\right) \qquad (20)$$

For the microstructures in this study, the g value for the equiaxed case was the average grain diameter of 24 μm, and in the columnar case, the average grain width was measured to be 100 μm. The liquid film thickness for both cases was normalized over the maximum columnar film thickness at the beginning of solidification and plotted against the square root of fraction solid in Fig. 7C. The columnar liquid channel width was much greater than the equiaxed channel width throughout the solidification of the alloys until they both converged at √fs = 1.

The Kou cracking susceptibility index was used to incorporate the effect of stresses/strains developed during solidification on the cracking response. Kou developed a cracking index that uses the maximum slope of an alloy's Scheil curve to predict its susceptibility to solidification cracking (Refs. 1, 25). When an alloy has a steep slope in its Scheil curve, it experiences little growth of the solid over a large temperature decrease, and there are large solidification thermal contraction stresses/strains that can accumulate without much solidification to accommodate the shrinkage. This condition can result in the development of stresses that separate the liquid films and cause solidification cracking. The Kou cracking index for 6061 aluminum normalized over its maximum value is also plotted in Fig. 7C. The values of the cracking index were very low for the majority of the solidification range until approximately $\sqrt{f_s} = 0.85$, where they increased greatly. Traditionally, the range where solidification cracking was expected to occur is $0.85 < \sqrt{f_s} < 0.99$ (Ref. 4) based on coarse columnar dendritic solidification of arc welds. Before $\sqrt{f_s} = 0.85$, the liquid films in a typical arc weld are large enough that the backfilling of any cracks is expected, and past $\sqrt{f_s} = 0.99$, there is extensive interdendritic bonding so that solidification cracks cannot propagate.

Over the critical film thickness range for columnar solidification corresponding to $0.85 < \sqrt{f_s} < 0.99$, the normalized crack index (assumed to be proportional to tensile stresses/strains) rapidly increases from ~ 0.02 to 1. Because the liquid films are thinner for all fractions of solid less than 1, the same

critical film thickness occurs at $\sqrt{f_s} < 0.85$ in the equiaxed case where the normalized cracking index is close to 0 and reaches a maximum of approximately 0.02 at roughly $\sqrt{f_s} = 0.85$. Under the assumption that the critical film thickness is the same for coarse columnar and fine equiaxed solidification, this model suggests that grain refinement suppresses solidification cracking by causing the critical film thickness to occur at lower fractions of solid where the solidification tensile stress/strains are much lower. Figure 7C also shows the normalized cracking index with a uniform increase for all fractions of solid that is meant to roughly approximate increased tensile stresses from the increased constraint that might be encountered in full penetration melt pools (like the high heat input welding parameters used here). Depending on the degree of external restraint, the stresses exerted on the microstructure while the critical film thickness is present in the equiaxed case can be high enough to cause cracking. In essence, the change in solidification morphology from coarse columnar to fine equiaxed does nothing to alter the inherent susceptibility of an alloy to solidification cracking (as represented by the normalized cracking index). In the finer equiaxed case, the critical film thickness occurs earlier in solidification when thermal stresses are lower, and sufficient intergranular bonding has occurred by the time high thermal stresses are expected later in the stages of solidification. Overall, this new model gives some insight into why increasing tensile stresses/strains during solidification through external restraint can overcome the solidification cracking suppression offered by finer equiaxed grain structures.

Comparison of Weldability Test Results to Fabrication Experience

Although inoculation in the GMA-DED material led to grain refinement in the GTA welds, cracking was induced with the test, which allowed for statistical analysis of the reduction in the degree of cracking. This result does not imply that welds made with the inoculated 6061 material will *always* crack. The same wire used to make the inoculated GMA-DED material was used to make crack-free multi-pass GTA groove welds (Ref. 12); however, the differences in the welding conditions compared to this work likely led to different transverse tensile stresses during solidification. When filler metal is used in multipass groove welds, the melt pools are often smaller, resulting in lower stresses, both due to lower heat inputs and less solidification shrinkage. Solidification shrinkage strains and thermal contractions are high in aluminum alloys, exerting significant strains in the solidified material (Refs. 2, 3). Additionally, most of the welds made in a multipass groove joint have material under them in the joint to accommodate the stresses during solidification. In contrast, in the full-penetration welds in this study, the entirety of the thermal and shrinkage stresses were experienced by the liquid melt pool, resulting in high transverse tensile stresses to drive solidification cracking. While cracking was induced in all the materials in this work using autogenous full penetration welds, based on existing work and the trends presented in this study, the inoculated 6061 material can be welded with GTAW and GMAW and

additively manufactured with GMA-DED. Still, care must be taken to minimize tensile stress during solidification. The results of the weldability test reported here provide crucial crack susceptibility information to design welding or AM processes to avoid cracking.

Conclusions

Weldability tests using autogenous GTAW were conducted on plain and inoculated GMA-DED 6061 materials and wrought 6061 to understand the effects of inoculation on the degree of cracking. A combination of heat transfer and microstructure development models were used to predict the grain structure in the GTA welds. A new model was developed to explain the relationship between grain refinement, tensile stresses during solidification, and solidification cracking. Based on the results, the following conclusions are made:

■ There is a statistically significant decrease in the amount of cracking observed in GTA welds made on inoculated GMA-DED 6061 material compared to plain GMA-DED and wrought 6061. There is no statistically significant difference in the degree of cracking observed in GTA welds on plain GMA-DED and wrought 6061.

■ The highest heat input condition resulted in no statistically significant change in cracking behavior between GTA welds on inoculated GMA-DED, plain GMA-DED, and wrought 6061. The highest heat input condition resulted in the widest melt pool, which likely had the highest magnitude of tensile stress during solidification.

■ A combination of heat transfer and microstructure development models was employed to predict the near equiaxed grain structure in the GTA welds on the inoculated GMA-DED material and the columnar grain structure in the welds made on the plain GMA-DED 6061 material. The refined microstructure of the GTA welds indicates that grain size refinement is still achieved after autogenous remelting of deposited inoculated material.

■ A model was developed in this work to account for the impact of solidification morphology, thermal stresses, and external tensile stresses on cracking susceptibility. The model suggests an equiaxed microstructure results in smaller liquid film thicknesses such that the window of critical liquid film thickness is shifted to slower fractions of solid where thermal stresses are lower. Moreover, sufficient bonding occurs between equiaxed grains to suppress cracking at higher fractions of solid where solidification stresses are the highest. However, increasing the magnitude of externally applied tensile stress where the critical liquid film thickness is present in equiaxed microstructures can promote solidification cracking.

■ Although grain refinement conclusively reduces the amount of solidification cracking, care must be taken to minimize tensile residual stresses by joint design in welds or print strategy and component design in additive manufacturing to minimize the chance for cracking in high strength aluminum alloys, such as 6061, that are inherently highly susceptible to solidification cracking.

■ The results of this work are expected to improve the design of new inoculated high strength aluminum alloys and improve welding and additive manufacturing process development.

Acknowledgments

Conflict of Interest

On behalf of all authors, the corresponding author states that there is no conflict of interest.

References

1. Kou, S. 2015. A criterion for cracking during solidification. *Acta Materialia* 88: 366–374.

2. Flemings, M. C. 1974. *Solidification Processing*. New York: McGraw Hill.

3. Eskin, D. G., Katgerman, L., Suyitno, and Mooney, J. F. 2004. Contraction of aluminum alloys during and after solidification. *Metallurgical and Materials Transactions A* 35: 1325–1335.

4. Kou, S. 2021. *Welding Metallurgy*, 3rd ed. New Jersey: John Wiley and Sons Inc.

5. Mousavi, M. G., Cross, C. E., and Grong, Ø. 1999. Effect of scandium and titanium–boron on grain refinement and hot cracking of aluminium alloy 7108. *Science and Technology of Welding and Joining* 4(6): 381–388.

6. Martin, J. H., Yahata, B. D., Hundley, J. M., Mayer, J. A., Schaedler, T. A., and Pollock, T. M. 2017. 3D printing of high-strength aluminium alloys. *Nature* 549(7672): 365–369.

7. Gradl, P., Waller, D., Fedotowsky, T., Johnson, C., and Williams, B. 2023. Advancing additively manufactured Al 6061 RAM2 using laser powder directed energy deposition. *8th Annual International Conference on Advanced Manufacturing*, Washington, D.C.

8. Tan, Q., Zhang, J., Sun, Q., Fan, Q., Li, G., Yin, Y., Liu, Y., and Zhang, M. 2020. Inoculation treatment of an additively manufactured 2024 aluminium alloy with titanium nanoparticles. *Acta Materialia* 196(1): 1–16.

9. Sullivan, E., Polizzi, A., Iten, J., Nuechterlein, J., Domack, M., and Liu, S. 2022. Microstructural characterization and tensile behavior of reaction synthesis aluminum 6061 metal matrix composites produced via laser beam powder bed fusion and electron beam freeform fabrication. *The International Journal of Advanced Manufacturing Technology* 121(3): 2197–2218.

10. Sokoluk, M., Cao, C., Pan, S., and Li, X. 2019. Nanoparticle-enabled phase control for arc welding of unweldable aluminum alloy 7075. *Nature Communications* 10(1): 98.

11. Jin, J., Geng, S., Shu, L., Jiang, P., Shao, X., Han, C., Ren, L., Li, Y., Yang, L., and Wang, X. 2024. High-strength and crack-free welding of 2024 aluminium alloy via Zr-core-Al-shell wire. *Nature Communications* 15(1): 1748.

12. Fedotowsky, T., Williams, B., Gradl, P. R., and Tinker, D. C. 2024. Al6061-RAM2 development and hot-fire testing using additive manufacturing laser powder directed energy deposition for liquid rocket engine channel-cooled nozzles. *AIAA SCITECH 2024 Forum*: 0994.

13. Nuechterlein, J., and Iten, J. Reactive additive manufacturing. U.S. Patent 10507638B2, filed March 15, 2016, and issued December 12, 2019.

14. Rosenthal, D. 1941. Mathematical theory of heat distribution during welding and cutting. *Welding Journal* 20(5): 220–234.

15. Florea, R. S., Bammann, D. J., Yeldell, A., Solanki, K. N., and Hammi, Y. 2013. Welding parameters influence on fatigue life and microstructure in resistance spot welding of 6061-T6 aluminum alloy. *Materials & Design* 45: 456–465.

16. Øystein, G. 1997. *Metallurgical modelling of welding*. The Institute of Materials.

17. Kleindienst, J., Bagshaw, N., Iten, J., and Klemm-Toole, J. 2025. Modeling solidification microstructure in an inoculated aluminum 6061 alloy processed with gas metal arc directed energy deposition. *JOM*. DOI: 10.1007/s11837-024-07066-4

18. Hagen, L., Yu, Z., Clarke, A., Clarke, K., Tate, S., Petrella, A., and Klemm-Toole, J. 2023. High deposition rate wire-arc directed energy deposition of 316L and 316LSi: process exploration and modelling. *Materials Science and Engineering: A* 880: 145044.

19. Kurz, W., Fisher, D. J., and Trivedi, R. 2019. Progress in modelling solidification microstructures in metals and alloys: dendrites and cells from 1700 to 2000. *International Materials Reviews* 64: 311–354.

20. Easton, M., Davidson, C., and St John, D. 2010. Effect of alloy composition on the dendrite arm spacing of multicomponent aluminum alloys. *Metallurgical and Materials Transactions A* 41: 1528–1538.

21. Dong, H. B., and Lee, P. D. 2005. Simulation of the columnar-to-equiaxed transition in directionally solidified Al–Cu alloys. *Acta Materialia* 53(3): 659–668.

22. Hunt, J. D. 1984. Steady state columnar and equiaxed growth of dendrites and eutectic. *Materials Science and Engineering* 65: 75–83.

23. Gäumann, M., Bezençon, C., Canalis, P., and Kurz, W. 2001. Single-crystal laser deposition of superalloys: Processing–microstructure maps. *Acta Materialia* 49: 1051–1062.

24. Joseph, A., Harwig, D., Farson, D., and Richardson, R. 2003. Measurement and calculation of arc power and heat transfer efficiency in pulsed gas metal arc welding. *Science and Technology of Welding and Joining* 8: 400–406.

25. Kou, S. 2015. A simple index for predicting the susceptibility to solidification cracking. *Welding Journal* 94(12): 374-s to 388-s.

JOSEPH KLEINDIENST and **JONAH KLEMM-TOOLE** (*jklemmto@mines.edu*) are with Colorado School of Mines, Golden, Colo. **NICK BAGSHAW** is with Fortius Metals Inc., Lafayette, Colo. **JEREMY ITEN** is with Elementum 3D, Erie, Colo.